Distinct chromatin regulators downmodulate meiotic axis formation and DNA break induction at chromosome ends

Adhithi R. Raghavan[1], Kieron May[2], Vijayalakshmi V. Subramanian[1,3], Hannah G. Blitzblau[1], Neem J. Patel[1], Jonathan Houseley[2], Andreas Hochwagen[1*]

Affiliations:

1. Department of Biology, New York University, New York, USA
2. Epigenetics Programme, Babraham Institute, Cambridge, UK
3. Department of Biology, IISER Tirupati, Tirupati, India

*Corresponding Author (andi@nyu.edu)

Current Affiliations: N.J.P. - Basecamp Research, London, UK

Abstract:

In many organisms, meiotic crossover recombination is suppressed near the extreme ends of chromosomes. Here, we identified two chromatin modifiers, the histone methyltransferase Dot1 and the Sir silencing complex, as regulators of this process in *Saccharomyces cerevisiae*. We show that the recombination-promoting axis proteins Red1 and Hop1, but not the axis-associated cohesin Rec8, are significantly reduced within 20 kb of telomeres compared to the chromosome interior. Dot1, which preferentially methylates histones in the chromosome interior, is required for this pattern by directing Red1 binding toward the chromosome interior. In parallel, the Sir complex suppresses the induction of meiotic DNA double-strand breaks (DSBs) at chromosome ends. Sir-dependent DSB suppression is independent of axis deposition and occurs in a chromosome end-specific manner that mirrors the spreading and transcriptional silencing activity of the complex, suggesting that the Sir complex suppresses DSB formation by limiting the openness of promoters, the preferred sites of meiotic DSB formation. We conclude that multiple chromatin-based mechanisms collaborate to achieve a robust reduction of meiotic recombination near chromosome ends.

Keywords: meiotic DSBs, subtelomeres, axis proteins, chromatin modifiers, Dot1, Sir2, Sir3

30 **Introduction:**

31 Meiosis is a specialized type of cell division that generates haploid gametes from diploid
32 progenitor cells and plays an essential role in promoting genetic diversity[1]. Meiosis initiates with
33 a single round of DNA replication followed by two rounds of chromosome segregation: the first
34 segregates homologous chromosomes, and the second segregates sister chromatids[2,3]. Accurate
35 segregation during meiosis I relies on meiotic crossover recombination, which exchanges DNA
36 between homologous chromosome pairs and, together with sister chromatid cohesion, forms a
37 physical connection between them[4]. Meiotic recombination is initiated by programmed double-
38 strand breaks (DSBs), which are catalyzed by Spo11, a highly conserved topoisomerase-like
39 enzyme[5].

40 Although DSBs can occur throughout the genome, their frequency varies widely. Chromosomal
41 regions classified as "hot" experience frequent DSBs, whereas "cold" regions rarely undergo
42 breakage[6]. This spatial regulation results from a complex interplay of factors, including local base
43 composition, DNA accessibility, chromatin modifications, and meiotic chromosome
44 architecture[5,7,8]. Meiosis-specific axis proteins, which localize at the base of the loop-axis structure
45 of meiotic chromosomes, are also linked to DSB activity and the subsequent homolog-directed
46 repair[6,9-11]. In *S. cerevisiae*, the axis proteins Red1 and Hop1 are required for both processes[11-
47 14], and elevated levels of Red1 and Hop1 correlate with increased DSB formation and markers of
48 crossover repair[15,16]. Red1 and Hop1 are recruited to the base of chromatin loops by the meiotic
49 Rec8 cohesin complex but can also bind directly to chromatin through the nucleosome-binding
50 activity of Hop1[14,15,17], leading to two independent modes of axis-dependent patterning of meiotic
51 recombination.

52 In budding yeast, DSB activity is notably reduced within ~20 kb from telomeres[18]. This depletion
53 is likely important for two reasons. First, the ends of chromosomes are enriched for repetitive DNA

54 sequences that are vulnerable to non-allelic homologous recombination (NAHR) and genome
55 rearrangements[19]. Second, crossovers near chromosome ends are less effective at forming
56 stable connections between homologous chromosomes and may lead to chromosome mis-
57 segregation if they are the sole link between homolog pairs[20]. Indeed, recombination events near
58 telomeres are linked to a higher risk of Trisomy 21 (Down syndrome) in humans[21,22].

59 *S. cerevisiae* chromosome ends consist of several distinct regions (**Fig. 1a**)[23,24]. In addition to
60 telomerase-templated telomeric repeats that cap chromosome ends, "telomere-associated
61 sequences" contain repetitive Y' and X elements, while the "subtelomeric domains" extend inward
62 for an average of about 20 kb from telomeres. Subtelomeric domains are relatively gene-poor
63 regions enriched in gene families[25,26]. The telomeric repeats and X elements recruit the
64 Sir2/Sir3/Sir4 histone deacetylase complex, establishing transcriptional silencing. This silent
65 chromatin can spread over limited distances into the subtelomeric domains[27]. The subtelomeric
66 domains, in turn, are defined by a unique chromatin signature, which includes a relative depletion
67 of active chromatin marks[25,28].

68 Previous studies of meiotic recombination in *S. cerevisiae* have consistently shown a depletion of
69 DSBs in X and Y' elements as well as in subtelomeric domains[10,18,29]. While the mechanisms
70 governing DSB suppression in X and Y' elements remain largely unexplored, the reduced DSB
71 levels in subtelomeric domains are accompanied by lower recruitment of DSB-promoting factors,
72 such as Rec114[30], and diminished abundance of the axis protein Hop1[31]. Hop1, which recruits
73 Rec114[11], is currently the most upstream regulator of recombination known to be depleted about
74 20 kb from the chromosome ends. However, the specific mechanisms controlling this altered
75 distribution of Hop1—and whether its depletion is the sole driver of suppressed recombination
76 near telomeres—are not understood.

77 **Results:**

The meiotic axis extends into the telomere-associated X and Y' sequences

Given the reduced axis protein enrichment near chromosome ends and their critical role in meiotic DSB formation and repair, we investigated how axis proteins interact with telomere-associated sequences and subtelomeric domains. These regions are often excluded from sequence-based analyses due to variations in telomere organization even among closely related yeast strains[24,32,33], and because the abundance of repetitive sequences and gene families creates challenges for uniquely assigning sequencing reads. Therefore, we tailored our analysis pipeline to account for these unique biological features. To reduce structural mapping artifacts, we mapped reads to high-quality end-to-end chromosome scaffolds of our experimental strain (SK1)[32], rather than the commonly used S288c reference. Further, by exclusively considering optimal matches, we maximized the number of confidently mapped reads, leveraging inherent sequence polymorphisms within telomeric repeat sequences for unique mapping. This approach resulted in high mapping success across all telomere-proximal regions **(Supplementary Fig. 1a)**. Even in the highly repetitive X and Y' elements, our pipeline uniquely mapped 12.81% and 0.87% of single-end reads and 15.18% and 12.80% of paired-end reads, respectively. In the subtelomeric domains, unique mapping rates were higher, averaging 24.07% for single-end reads and 32.21% for paired-end reads.

If a read had multiple equally good mapping results, our pipeline randomly selected one location as the primary alignment for the read. This approach did not affect metagene analyses but significantly improved signal clarity at individual chromosome ends by closing coverage gaps caused by a lack of polymorphisms. Comparative analysis of profiles with and without multiple mapping reads revealed no qualitative differences **(Supplementary Fig. 1b)**, supporting the robustness of our approach.

101 With this strategy, we analyzed the distribution of axis proteins at chromosome ends using
102 previously published ChIP-seq datasets[14,31,34]. Meta-analysis revealed that Red1 and Hop1 were
103 significantly less enriched than the genome average within 20 kb of chromosome ends **(Fig. 1b-**
104 **c)**, consistent with previous studies[31]. Axis protein depletion was observed across all chromosome
105 ends, and thus could not be attributed to individual telomere outliers **(Supplementary Fig. 2)**.

106 Yeast chromosome ends are characterized by telomeric repeats, $(TG_{1-3})_n$, and telomere-
107 associated sequences, which include the Y' and X elements[35]. The long Y' elements (4-7 kb) are
108 not found on all ends and can occur as one or multiple copies, whereas a short X element (~500
109 bp) is present at essentially all chromosome ends[32,36] **(Fig. 1a)**. Based on these features, we
110 classified chromosome ends into two categories: X-only ends, which contain only the X element,
111 and XY' ends, which include both X and Y' elements. Meta-plots of Red1 and Hop1 profiles
112 revealed that axis protein enrichment differed between these two categories. X elements at X-
113 only ends exhibited axis protein enrichment close to the genome average, indicating that isolated
114 X elements have a substantial propensity for axis protein recruitment **(Fig. 1d)**. By contrast, X
115 elements at XY' ends showed Red1 and Hop1 enrichment below the genome average **(Fig. 1d),**
116 suggesting that the presence of Y' elements reduces axis protein binding on adjacent X elements
117 **(Fig. 1f)**. This reduction may result from axis protein repositioning, as meta-analyses revealed an
118 axis protein binding site at the telomere-proximal side of the Y' element **(Fig. 1e).**

119 **Multiple *cis*-acting features contribute to axis protein depletion near telomeres**

120 Altered axis protein binding on adjacent X elements suggests that Y' sequences may partially
121 drive the telomere-proximal depletion of axis proteins observed in our meta-analysis **(Fig. 1b-c)**.
122 In support of this, although both XY' and X-only chromosome ends show reduced axis protein
123 binding compared to the genome average, the depletion is stronger at XY' ends **(Fig. 2a)**. These
124 results indicate that Y' elements contribute to the overall reduction of axis proteins at chromosome

125 ends. However, the observation that axis protein levels are also lower at X-only ends implies that
126 additional mechanisms further suppress axis protein recruitment near telomeres.

127 To determine whether this additional mechanism is due to telomere proximity or intrinsic
128 sequence features, we analyzed chromosome fusions, in which subtelomeric domains were
129 relocated to the chromosome interior[37]. We observed that axis protein distribution at fused
130 chromosome ends mirrored that of native, unfused ends **(Fig. 2b)**, suggesting that reduced axis
131 protein enrichment at chromosome ends is driven by specific sequences encoded at chromosome
132 ends rather than by telomere proximity.

133 Across the genome, gene-rich regions exhibit an overall higher axis protein enrichment[14,15]. As
134 the subtelomeric domains are comparatively gene-poor[25,26], we plotted coding density (the
135 fraction of DNA encoding open reading frames) as a function of distance from the telomeres. This
136 analysis revealed a strong correlation between the regions of reduced coding density and axis
137 protein depletion **(Fig. 2c)**, suggesting that reduced coding density may partially underlie the
138 reduced axis protein recruitment within 20 kb of telomeres.

139 **Rec8-dependent and independent pathways mediate axis protein localization at**
140 **chromosome ends**

141 Chromosomal recruitment of Red1 and Hop1 is mediated by two parallel pathways. The meiotic
142 Rec8-cohesin complex preferentially recruits axis proteins to sites of convergent transcription[14],
143 whereas the chromatin binding region (CBR) of Hop1 directs axis proteins to nucleosome-dense
144 regions—“islands” characterized by higher coding density[15,17]. We sought to determine whether
145 the depletion of axis proteins near chromosome ends could be attributed to the inactivity of one
146 of these pathways.

147 Analysis of ChIP-seq data revealed that Rec8 is abundantly present at chromosome ends. Unlike
148 Red1 and Hop1, Rec8-cohesin levels in the subtelomeric regions were comparable to the genome
149 average **(Fig. 1b, c)**. Moreover, the regions enriched for Red1 and Hop1 in the telomere-
150 associated sequences were also enriched for Rec8: Rec8 was bound more strongly to the X
151 elements of X-only ends than to XY' ends **(Fig. 1d, f)** and formed a strong peak at the telomere-
152 proximal side of Y' elements **(Fig. 1e)**. This peak coincided with the 3' end of the Y'-encoded open
153 reading frame (ORF), consistent with other chromosomal Rec8 peaks, which are typically
154 enriched downstream of ORFs[14,38]. Previous studies have demonstrated that active transcription
155 can induce the sliding of the cohesin ring and direct axis protein association to the end of
156 ORFs[14,39,40]. Therefore, transcription of the Y' ORF may similarly influence axis protein deposition
157 within Y' elements.

158 The coincident binding of axis proteins and Rec8 supports the hypothesis that Rec8-cohesin is
159 an important contributor to axis protein deposition at chromosome ends. To directly test this
160 possibility, we examined Red1 binding in a *rec8* mutant strain using spike-in normalized ChIP-
161 seq datasets[15,34]. In the subtelomeric domains, Red1 levels were significantly reduced in the *rec8*
162 mutant compared to wild-type (**Fig. 3a-b**). However, Red1 binding was still detectable above
163 baseline levels. Axis protein binding in the absence of Rec8 depends on the CBR domain of
164 Hop1[15,17]. Indeed, the persistent subtelomeric axis protein signal in *rec8* mutants was abolished
165 upon introduction of a Hop1 mutant (*hop1-phd*) lacking the CBR[15,17] **(Fig. 3a-b)**. By contrast, the
166 *hop1-phd* mutation alone had comparatively minor effects in the subtelomeric domains, although
167 we consistently noted reduced Red1 binding in the neighboring end-adjacent regions (EARs, 20-
168 120 kb)[31] **(Fig. 3a-b)**. These data indicate that both pathways of axis recruitment additively
169 contribute to Red1 binding at chromosome ends, with Rec8-cohesin responsible for recruiting the
170 majority of Red1, consistent with the low coding density in these regions **(Fig. 2c)**. Similar additive

171 effects were observed in the X and Y' sequences **(Fig. 3c, d)**. Therefore, the selective inactivation
172 of one recruitment pathway cannot explain the depletion of axis proteins in subtelomeric domains.

173 **The methyltransferase Dot1 is required for subtelomeric depletion of axis proteins**

174 Subtelomeric regions share qualitative similarities with pericentromeric regions, particularly in the
175 differential enrichment of axis proteins and Rec8-cohesin. Both regions show a relatively higher
176 abundance of Rec8-cohesin compared to Red1, with most data points falling below the genome-
177 wide regression line **(Fig. 4a).** At pericentromeres, this differential enrichment of axis factors
178 persists even if the centromere itself is inactivated[37], indicating that local DNA or chromatin
179 environment influences axis protein binding. Given the distinct chromatin state of subtelomeric
180 domains, we investigated whether chromatin modifiers specific to these regions contribute to axis
181 protein depletion.

182 We focused our analysis on histone marks related to meiotic DSB formation[41,42] or those
183 specifically different in the subtelomeric domains[28,42-44]. ChIP-seq analysis identified two marks -
184 H3K4me3 and H3K79me3 - that closely matched the pattern of axis protein depletion **(Fig. 4b)**.
185 Both marks are long-lasting indicators of active gene expression that are depleted from
186 subtelomeric domains in vegetative cells [25,28] and have been implicated in the control of meiotic
187 DSB formation[41,45]. To explore the role of these histone modifications in axis protein depletion, we
188 used spike-in normalized ChIP-seq to analyze Red1 in mutants lacking Set1 or Dot1, the enzymes
189 responsible for the trimethylation of H3K4 and H3K79, respectively[34]. In *set1Δ* mutants,
190 subtelomeric Red1 binding patterns were indistinguishable from wild-type **(Fig. 4c-e)**. In contrast,
191 Red1 levels in *dot1Δ* mutants were markedly elevated and no longer significantly different from
192 the genome average **(Fig. 4c-e)**, suggesting that Dot1 suppresses axis protein binding in
193 subtelomeric domains. Red1 levels were also elevated across Y' elements and moderately over
194 X elements **(Fig. 4g, h)**. Notably, pericentromeric axis protein recruitment in *dot1Δ* mutants did

195 not show a statistically significant difference by bootstrapping analysis, although the average
196 binding values were slightly reduced compared to wild-type **(Fig. 4f)**. In contrast, subtelomeric
197 regions exhibited the opposite effect, with average binding levels increasing in *dot1Δ* mutants
198 **(Fig. 4e)**.

199 Subtelomeric regions in wild-type cells are undermethylated on H3K79 **(Fig. 4b)**, suggesting that
200 the role of Dot1 in axis protein regulation may be indirect. In line with this interpretation, spike-in
201 normalized ChIP-seq data showed that the increased Red1 binding in subtelomeric regions of
202 *dot1Δ* mutants was accompanied by lower Red1 levels in the chromosome interior **(Fig. 4c-e)**.
203 To probe which axis recruitment pathway is regulated by Dot1, we separated Red1 signals into
204 genic and intergenic regions, as Hop1 primarily recruits Red1 to gene bodies, whereas Rec8-
205 cohesin leads to Red1 enrichment in intergenic regions[14]. The reduced binding of Red1 in the
206 chromosome interior in *dot1Δ* mutants primarily affected intergenic regions, implying that Dot1
207 promotes Rec8-dependent axis binding. Consistent with this interpretation, the increase in Red1
208 association near chromosome ends in *dot1Δ* mutants occurred predominantly on gene bodies
209 **(Fig. 4i)**. These data indicate that the chromatin requirements for axis recruitment differ between
210 chromosome ends and the chromosome interior, and that Dot1 helps direct Red1 to chromosome
211 interiors by promoting Rec8-dependent axis recruitment.

212 **Conservation of Sir-dependent telomeric heterochromatin during meiotic recombination**

213 One consequence of *DOT1* disruption is the spreading of the Sir complex beyond its usual
214 boundaries[46,47]. Indeed, the mislocalization of Sir2 and Sir3 in *dot1* mutants was previously linked
215 to checkpoint defects during meiotic recombination[48]. To investigate this link further, we examined
216 the role of the Sir complex in suppressing axis protein deposition and DSB formation at
217 chromosome ends.

218 In vegetative cells, the Sir complex establishes silent chromatin domains at mating-type loci and
219 telomere-associated sequences[49,50]. At some chromosome ends, Sir chromatin also spreads from
220 the X element into the neighboring subtelomeric domains[27,51], although spreading across entire
221 subtelomeric domains is only observed under conditions of Sir overexpression[28]. We used ChIP-
222 seq analysis to assess Sir3's chromatin association and spreading during meiotic prophase.

223 Our observations at the time of meiotic induction and during the peak of DSB formation (3 hours
224 post-induction) revealed consistent binding patterns **(Fig. 5a)**. Although Sir3 was enriched at both
225 types of X elements, its binding on X elements at XY' ends was lower than that observed at X-
226 only ends **(Fig. 5a, c)**. Sir3 was also enriched upstream of the Y'-encoded ORF, but binding was
227 relatively diminished across the Y' ORF **(Fig. 5b)**. Additionally, we observed heterogeneous
228 spreading of Sir3 from subtelomeric X elements into adjacent subtelomeric domains on certain
229 chromosome ends. For example, on chrVII-L, Sir3 spread approximately 6 kb from the X element
230 during early prophase I (3 hours post-meiotic induction) **(Fig. 5d)**, while there was no apparent
231 spreading on chrVI-L **(Fig. 5e)**. The extent of Sir3 spreading varied substantially and did not
232 correlate with the presence of Y' elements but mirrored the distribution of Sir proteins in vegetative
233 cells[27,28]. These findings indicate that Sir-dependent telomeric heterochromatin remains largely
234 unchanged as cells initiate meiotic recombination.

235 **Sir3 spreading into subtelomeric domains suppresses meiotic transcription but does not**
236 **affect axis protein deposition.**

237 To determine whether subtelomeric domains with Sir3 spreading exhibit altered transcription of
238 underlying genes, we conducted mRNA-seq analysis on samples collected 3 hours post-meiotic
239 induction in the presence or absence of *SIR3*. Plotting relative fold changes in mRNA levels as a
240 function of the average Sir3 occupancy in the associated promoter region (250bp upstream of
241 each gene), revealed a significant correlation between Sir3 occupancy and increased mRNA

242 levels upon *SIR3* deletion **(Fig. 6a**) in the 5 kb regions adjacent to the X element where Sir3
243 frequently spreads. These results indicate that the transcriptional effects of Sir3 are confined to
244 sequences where Sir3 spreading occurs, as detected by ChIP-seq.

245 Given the prominent Sir3 peak observed at the start of the Y' element metaplot **(Fig. 5b)**, we also
246 analyzed Y' element expression at 3 hours post-meiotic induction. The average Y' element
247 expression was significantly increased in the absence of *SIR3* **(Supplementary Fig. 3**). These
248 results suggest that the absence of *SIR3* impacts Y' element transcription.

249 We asked whether deletion of *SIR3* also affects the deposition of axis proteins near chromosome
250 ends by determining the distribution of Red1 in *sir3* mutants using spike-in normalized ChIP-seq
251 analysis. Meta-analysis revealed no significant difference in the average depletion of Red1 in the
252 last 20 kb between *sir3* and wild-type strains **(Supplementary Fig. 4a, b)**. Similarly, meta-plots
253 of average Red1 profiles on X and Y' elements in *sir3* mutants showed no new peaks compared
254 to wild-type **(Supplementary Fig. 4c, d)**, although enrichment levels were lower on both types of
255 X element **(Supplementary Fig. 4c)**. The overall genome-wide median binding levels of Red1
256 were higher in the *sir3* mutants **(Supplementary Fig. 4b)**, aligning with the previously reported
257 analyses of Hop1[31]. These findings indicate that Sir3 binding, and the establishment of silent
258 chromatin domains do not result in large-scale alterations to the binding landscape of axis proteins
259 at chromosome ends. They also imply that the altered axis protein binding seen in *dot1* mutants
260 is not a consequence of the increased Sir complex spreading in this mutant.

261 **Sir proteins protect X elements and regions of Sir spreading from meiotic DSBs**

262 We wondered how Sir-dependent heterochromatin and Dot1-dependent axis protein suppression
263 interface with the meiotic DSB machinery near chromosome ends. Genome-wide DSB levels had
264 previously been determined in *sir2Δ* strains using Spo11-oligo sequencing, which sequences the
265 DNA fragments that remain covalently attached to Spo11 after cleavage[31,52], but telomere-

266 proximal DSB formation had not been investigated in that study. Analysis of this dataset revealed
267 a significant increase in DSB levels on X elements but not on Y' elements in *sir2Δ* strains **(Fig.**
268 **6b**). This pattern mirrors the relative enrichment of Sir3 in these elements, indicating that Sir
269 chromatin suppresses DSB formation in the X elements.

270 We also observed increased DSB formation in the subtelomeric domains in *sir2Δ* mutants.
271 Increased DSB induction was correlated with the extent of Sir3 occupancy in wild-type cells **(Fig.**
272 **6c)**. Accordingly, increased DSB formation also correlated with elevated gene expression in the
273 same regions in *sir3* mutants but not in the rest of the genome **(Fig. 6d)**. These findings suggest
274 that elevated promoter openness, which enables increased gene expression, also creates a
275 window for meiotic DSB formation.

276 To complement and expand this analysis, we analyzed *sir3* and *dot1Δ* mutants by TrAEL-seq,
277 which sequences the exposed 3' ends that result from Spo11 removal[53]. To avoid signal changes
278 due to DSB repair, this analysis was conducted in a repair-defective *dmc1Δ* background[54]. TrAEL-
279 seq analysis at the 5-hour time point showed a distinct increase in DSB formation within 20 kb of
280 telomeres in *sir3* mutants, with the number of significant DSB hotspots nearly doubling within 5
281 kb of X elements **(Fig. 6e, f)**. On the other hand, DSB formation was unaffected in the same
282 regions in *dot1Δ* mutants **(Fig. 6e, f)**. Accordingly, TrAEL-seq analysis of *sir3 dot1Δ* double
283 mutants revealed DSB patterns similar to *sir3* single mutants **(Fig. 6e, f)**. Moreover, a substantial
284 level of DSB suppression persisted even in the double mutant **(Fig. 6e, Supplementary Fig. 5b)**,
285 indicating that additional layers of regulation contribute to DSB suppression at chromosome ends
286 (see Discussion).

287 Intriguingly, TrAEL-seq analysis indicated differing genetic interactions between *DOT1* and *SIR3*
288 in other parts of the genome. DSB levels dropped in the subtelomere-adjacent EARs, specifically
289 in *dot1Δ sir3* double mutants, suggesting redundant functions **(Supplementary Fig. 5a)**, whereas

290 DSB formation around centromeres was decreased to a similar extent in *dot1Δ* and *sir3* single
291 mutants **(Supplementary Fig. 5b)**. Finally, around the ribosomal DNA locus, DSB levels were
292 increased in a Sir3-dependent manner in *dot1Δ* mutants **(Supplementary Fig. 5c)**, consistent
293 with previously observed Sir-dependent DSB induction in this region[55]. These findings imply a
294 combinatorial code that allows these two chromatin regulators to adjust meiotic recombination in
295 a region-specific manner.

296 **Discussion:**

297 Here we show that meiotic recombination potential at chromosome ends is suppressed by at least
298 two mechanisms. First, the local depletion of axis proteins, which regulate the recruitment of key
299 DSB factors and help target DSBs toward recombination with the homologous chromosome.
300 Second, telomeric heterochromatin restricts access to gene promoters, the preferred DNA
301 substrates for DSB formation in yeast[10] **(Fig. 7)**. These mechanisms thus represent distinct
302 strategies for regulating meiotic recombination potential.

303 The range of these two mechanisms differs significantly. Dot1-dependent axis protein depletion
304 spans the entire subtelomeric domain and exhibits consistent patterns across chromosome ends,
305 with variability largely driven by the distribution of axis binding sites[14]. In contrast, Sir-dependent
306 DSB suppression is highly variable among chromosome ends, driven by the extent of Sir-
307 dependent chromatin spreading. This variability in heterochromatin spread is also observed in
308 vegetative cells, where boundaries are influenced by transcription factor binding sites, genic
309 elements, and nucleosome-disfavoring DNA sequences [25,56-60].

310 While Sir-dependent chromatin spreading directly suppresses DSB hotspots, Dot1 likely
311 influences axis deposition indirectly **(Fig. 7)**, as H3K79 trimethylation occurs predominantly in the
312 chromosome interior[25]. Our findings demonstrate that the *dot1Δ* mutation causes a genome-wide
313 redistribution of Red1, with reduced binding in the chromosomal interior. Because Red1 levels

314 are limiting[61], one potential explanation is that the absence of Dot1 releases Red1 from intergenic
315 regions, enabling it to bind gene bodies in the subtelomeric domains **(Supplementary Fig. 6)**.
316 Intriguingly, the *hop1-phd* mutant, which should also release some Red1 because of its failure to
317 bind to gene bodies across the genome[15], does not exhibit similar increases in Red1 binding at
318 subtelomeric domains **(Fig. 2a)**, raising the possibility that the increased axis recruitment to
319 subtelomeric domains in *dot1Δ* mutants requires the CBR domain.

320 Although subtelomeric regions in *dot1Δ* mutants exhibit increased DSB potential due to Red1
321 redistribution, this does not result in substantial increases in DSB formation, even in *sir3 dot1Δ*
322 double mutants in which the suppressive effect of the Sir complex is eliminated. We speculate
323 that the absence of a stronger effect may be the consequence of increased DSB turnover, which
324 would not be detected by our TrAEL-seq analyses. Dot1 is required for the meiotic arrest of *dmc1Δ*
325 mutants[48]. As a result, repair foci disappear in *dot1Δ dmc1Δ* mutants as cells progress into
326 meiosis I, with breaks repaired via Rad54-dependent inter-sister recombination[48]. Moreover,
327 additional regulatory layers of telomere-proximal DSB suppression must exist because a
328 significant level of DSB suppression persists even in *sir3 dot1Δ* double mutants. These layers
329 may include further chromatin-based mechanisms. Additionally, one likely contributor is the low
330 coding density of subtelomeric regions as the lower density of gene promoters inherently results
331 in a smaller number of potential DSB hotspots. Indeed, the regional drop in coding density
332 correlates well with reduced axis protein recruitment and DSB formation. Our analysis of axis
333 deposition in chromosome fusion strains also supports this notion. Thus, to some extent the low
334 DSB potential may be hardwired into the genome sequence of chromosome ends. The combined
335 action of multiple pathways suppressing recombination at chromosome ends likely ensures that
336 meiotic crossovers are strongly disfavored near telomeres. Telomere-proximal crossovers are
337 less effective at maintaining linkages between homologous chromosomes[62] and are associated
338 with increased risk of Down syndrome in humans[21,22,63,64]. The downmodulation of axis proteins

339 in subtelomeric regions may play a critical role in this process, as axis proteins not only recruit
340 DSB factors but also help target DSB repair to homologous chromosomes by preventing sister
341 chromatid recombination[65]. Although a low level of DSBs occurs in telomere-associated regions
342 and subtelomeric domains[10], reduced axis protein abundance likely makes these regions less
343 prone to crossover formation. Favoring repair from sister chromatids may also reduce the risk of
344 non-allelic recombination events. Non-allelic recombination is especially risky at chromosome
345 ends due to their repetitive sequences and the close physical proximity of telomeres along the
346 nuclear envelope during meiotic prophase[19,66,67]. These multiple regulatory layers thus establish
347 a robust protective mechanism to shield chromosome ends from non-allelic and unproductive
348 recombination and ensure proper meiotic chromosome segregation.

349 **Methods and Materials:**

350 **Yeast strains and growth conditions:**

351 All the strains utilized in this study belonged to the SK1 background (except for the analysis using
352 the published fusion chromosomes, which are SK1 and S288C hybrids). The genotypes are
353 detailed in **Supplementary Table 1.** For experiments using vegetative cells, mid-logarithmic
354 phase cultures were grown in YPD medium overnight at room temperature until saturation. On
355 the following day, the cells were diluted to an OD600 of 0.2 and incubated at 30°C until they
356 reached an OD600 of 1. At this stage, 50 ml of culture was collected for ChIP-seq.

357 To induce synchronous meiotic cultures, strains were grown for 24 hours in YPD medium at room
358 temperature. Cells were enriched in the G1 phase by inoculating them at OD600 = 0.3 in pre-
359 sporulation BYTA medium (1% yeast extract, 2% bactotryptone, 1% potassium acetate, 50 mM
360 potassium phthalate) for 16.5 hours at 30°C. Cells were washed twice with sterile water and
361 transferred into SPO medium at OD600 = 1.9 (SPO: 0.3% potassium acetate, 0.001% acetic
362 acid). Cultures were grown at 30°C on a shaker, and the time of inoculation into SPO was defined

363 as time = 0. At specific timepoints, 25 ml of culture was collected for ChIP-seq and 1.6 ml for
364 mRNA-seq. The synchrony of meiotic cultures was validated using Fluorescence-activated cell
365 sorting (FACS).

366 **FACS:**

367 Cells collected at various timepoints were fixed overnight at 4°C in 350 µl of absolute ethanol.
368 Cells were pelleted and incubated in 500 µl FACS buffer (50 mM sodium citrate) with 0.7 µl RNase
369 A (20–40 mg/ml stock; Sigma-Aldrich) and 5 µl proteinase K (20 mg/ml; VWR) for 24 hours at
370 50°C. Prior to FACS analysis, cells were stained with 0.1 µl SYTOX Green (5 mM solution in
371 DMSO; Invitrogen) and briefly sonicated for 5 seconds at 10% amplitude. DNA content was
372 analyzed using the BD FACSAria II system at the Genomics Core at New York University Center
373 for Genomics and Systems Biology.

374 **Chromatin immunoprecipitation (ChIP) & Illumina sequencing:**

375 The cells collected at the indicated timepoints were pelleted and immediately crosslinked for 30
376 minutes in a 1% formaldehyde solution at room temperature with gentle shaking. Subsequently,
377 the crosslinking reaction was quenched by incubating the cells for 5 minutes at room temperature
378 in a 125 mM glycine solution. Following this, the cells were processed according to the protocol
379 outlined in[68] and immunoprecipitated with 2.5 µl of either anti-Sir3 (HM01065, a kind gift from the
380 Bell lab) or anti-Red1 (#16440, kind gift of N. Hollingsworth) or anti-H3K79me3 (abcam, ab2621).
381 Library preparation, quality, and quantity checks were then performed as described in [17]. All the
382 prepared chromatin immunoprecipitation (ChIP) libraries were sequenced as 150-bp paired-end
383 reads on Illumina NextSeq 500 instruments. The sequencing run was conducted by the Genomics
384 Core at New York University Center for Genomics and Systems Biology.

385 **Processing ChIP -seq reads from Illumina sequencing:**

386 Illumina sequencing reads were aligned to the SK1 genome[32] using Bowtie 2 (Version 2.4.2)[69].
387 To improve mapping of reads to repetitive subtelomeric regions, the Bowtie 2 read reporting mode
388 was configured to allow multiple alignments, reporting the best match[69]. MACS2 2.1.1 was used
389 to extend reads in the 5'-> 3' direction to a final length of 200 bp. SPMR (signal per million reads)
390 normalization was applied to both Input and ChIP pileups using MACS2. The resulting fold-
391 enrichment files were used for downstream analysis in R. The ChIP-seq pipeline and analysis
392 scripts are available on the Hochwagen Lab GitHub page
393 https://github.com/hochwagenlab/ChromosomeEnds.git.

394 **mRNA-sequencing & analysis:**

395 mRNA extraction, first- and second-strand synthesis, and library preparation were conducted
396 following the procedures outlined in[70]. The resulting libraries were subjected to sequencing as
397 150-bp paired-end reads on Illumina NextSeq 500 instruments. The sequencing run was executed
398 by the Genomics Core at New York University Center for Genomics and Systems Biology. The
399 GTF (General Transfer Format) file was modified to include all completely annotated Y' elements.
400 Subsequently, reads obtained from Illumina sequencing were aligned to the SK1 genome[32], and
401 the counts mapping to the modified SK1 gtf file were determined using the nf-core RNA-Seq
402 pipeline[71,72]. The relative abundances, measured as Transcripts per million (TPM) in the Salmon[73]
403 output file "salmon.merged.gene_counts_length_scaled.rds", were utilized for downstream
404 analysis in R.

405 **Spo11-oligos mapping:**

406 In this study, previously published Spo11-oligos datasets from WT and *sir2Δ* strains[31,52] were
407 utilized. Adaptors were removed from the reads using fastx_clipper from the FASTX-Toolkit
408 (version 0.0.14) and reads shorter than 15 bp were discarded. Subsequently, the clipped reads
409 were aligned to the SK1 genome[32] using Bowtie 2 (Version 2.4.2)[69] . The read alignment mode

410 was set to local, and the reporting mode allowed multiple read alignments while reporting the best
411 alignment[69]. Following alignment, MACS2 2.2 (https://github.com/taoliu/MACS) was employed to
412 extend reads in the 5'→3' direction to a final length of 37 bp[74]. SPMR (signal per million reads)
413 normalization was performed on the pileups.

414 **Plug preparation for TrAEL-seq:**

415 Plugs were prepared from meiotic cultures harvested 5 hours into meiosis. For each strain, 20 ml
416 of culture was pelleted and washed twice with CHEF TE buffer (10 mM Tris-HCl, pH 7.5, 50 mM
417 EDTA, pH 8.0). The cell pellet was resuspended in 300 µl CHEF TE, followed by the addition of
418 4 µl zymolyase (10 mg/ml). The mixture was briefly vortexed and incubated at 42°C for
419 approximately 30 seconds. Low-melting-point agarose (1% SeaPlaque GTG in 125 mM EDTA,
420 pH 8.0), prewarmed to 42°C, was added and transferred into plug molds. Plugs were solidified on
421 ice for 10 minutes before being transferred into LET buffer (10 mM Tris-HCl, pH 7.5; 0.5 M EDTA,
422 pH 8.0). Plugs were incubated overnight at 37°C.

423 The following day, plugs were treated with proteinase K in NDS buffer (10 mM Tris-HCl, pH 7.5;
424 0.5 M EDTA; 1% N-lauroylsarcosine) at 50°C overnight. After digestion, plugs were washed
425 sequentially: first with CHEF TE for 1 hour at room temperature, followed by two washes with
426 CHEF TE containing 10 µl freshly prepared PMSF (100 mM) in ethanol, with each wash incubated
427 for 1 hour in the cold room. A fourth wash was performed with RNase T1 in CHEF TE, incubated
428 at 37°C for 1 hour, followed by a final wash with CHEF TE at room temperature for 1 hour. Plugs
429 were stored at 4°C in CHEF TE until further use.

430 **TrAEL-seq Library Preparation, Sequencing, and Data Analysis:**

431 TrAEL-seq library preparation, sequencing and data analysis were conducted following the
432 procedures outlined in [53]. TrAEL-seq signal pileups were generated using MACS2 (v2.2) and

433 normalized pileups were generated using SPMR normalization. Downstream analyses were done
434 in R.

435 **Supporting information:** Supplementary Figures and Tables are attached in a word document.

436 **Data reporting:** The datasets generated and analyzed in this paper, excluding published
437 datasets, have been deposited in the Gene Expression Omnibus (GEO). The datasets can be
438 accessed with the accession number for ChIP-seq: GSExxxxxx, for RNA-seq: GSExxxxxx, and
439 for TrAEL-seq: GSExxxxxx. Additionally, all ChIP-seq datasets used in this study are described
440 in **Supplementary Table 2**, and all Spo11-oligos, RNA-seq and TrAEL-seq datasets are
441 described in **Supplementary Table 3**.

442 **Conflict of interest:** The authors declare no conflicting interests.

443 **Acknowledgements:**

444 We express our sincere gratitude to Stephen P. Bell for generously providing the Sir3 antibody
445 and to Nancy Hollingsworth for the Red1 antibody. We also acknowledge the Genomics Core at
446 the New York University Center for Genomics and Systems Biology for their valuable technical
447 assistance and expertise in data processing. This work was supported in part by the NYU IT High-
448 Performance Computing resources, services, and staff expertise. We are grateful to the Zegar
449 Family Foundation for their generous support. TrAEL-seq library sequencing and processing were
450 performed by the Genomics (Geno06) and Bioinformatics (Bioinf01) teams at the Babraham
451 Institute, which receive financial support from the Institute Core Capability Grant (BBSRC CCG).
452 This research was financially supported as part of NIH grant R35 GM148223 to AH. ARR
453 acknowledges support from a Fleur Strand Graduate Fellowship from the Department of Biology,
454 as well as a Henry MacCracken Fellowship and a Dean's Dissertation Fellowship from the NYU
455 Graduate School of Arts and Science. JH acknowledges funding from the BBSRC (BI Epigenetics

ISP; BBS/E/B/000C0523), and KM acknowledges funding from the BBSRC (BB/W509917/1). The funders had no role in the preparation of this manuscript.

Author contributions: Conceptualization - A.R.R., V.V.S., H.G.B., and A.H; Investigation & Formal analysis - A.R.R., K.M., V.V.S., H.G.B., N.J.P., J.H., A.H; Computational Pipeline development - A.R.R.; Manuscript writing (initial draft) - A.R.R. and A.H.; Manuscript editing - all authors.

Figures:

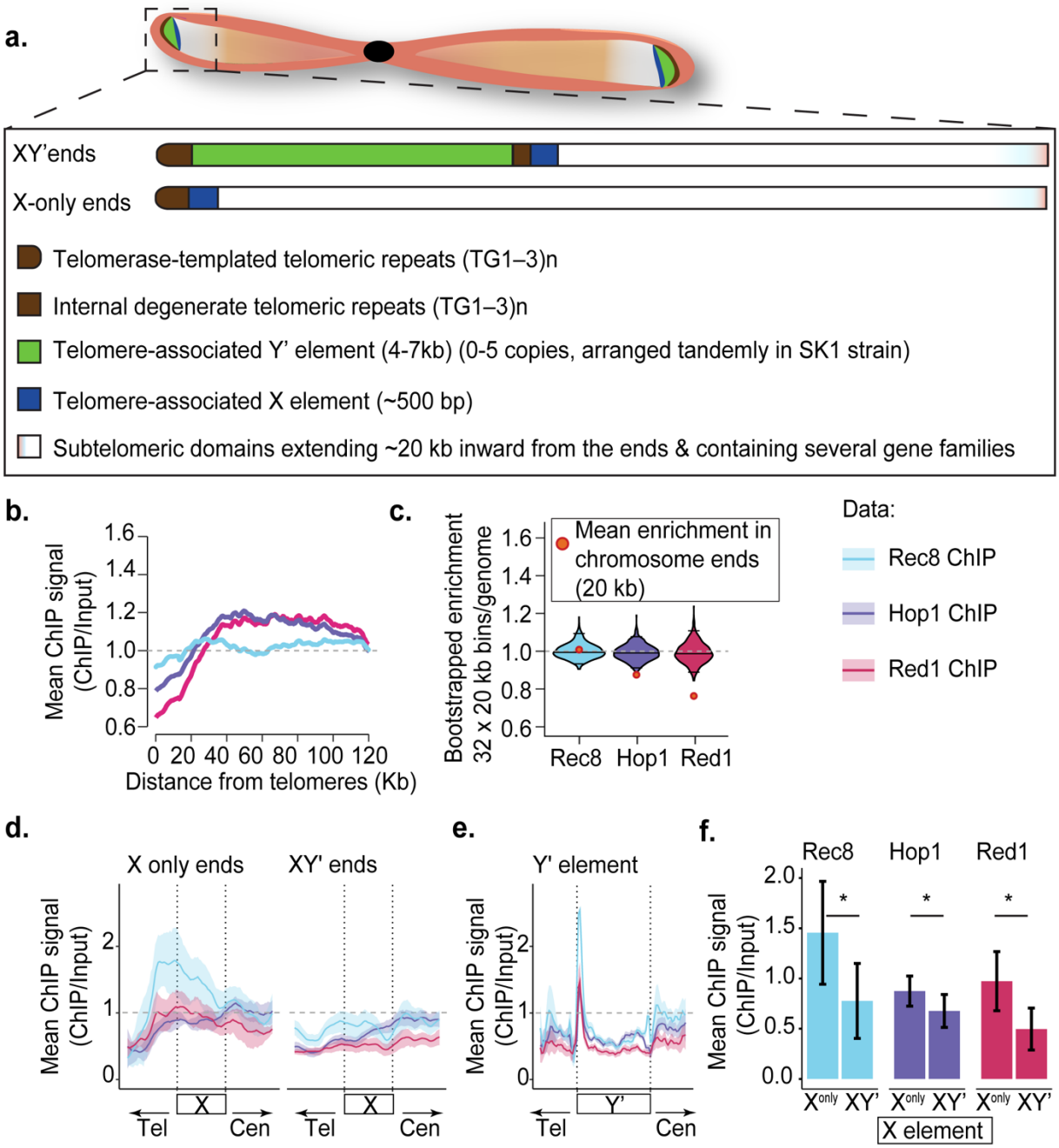

Raghavan *et al*, Fig. 1

Fig. 1: Meiotic axis extends to the telomere-associated sequences. (a) Schematic representation of the distinct regions present at chromosome ends in *Saccharomyces cerevisiae*. Black dot represents the centromere. **(b)** Mean fold enrichment of Rec8, Red1, and Hop1 relative to their distance from telomeres, using published ChIP-seq datasets from WT cells at early

470 prophase I (3 hours)[14]. **(c)** Bootstrapped distributions of fold enrichment within thirty-two 20 kb
471 bins spanning the genome. Median values and two-sided 95% confidence intervals are shown as
472 black horizontal lines, with orange/red circles highlighting the mean enrichment in the last 20 kb
473 of chromosome ends. **(d, e)** Meta-plots of average Rec8, Red1, and Hop1 enrichment at
474 chromosome end-associated X and Y' elements. Vertical dotted lines mark the positions of the X
475 or Y' element. For X elements, regions of equal size adjacent to the X element on both the
476 centromere-proximal (Cen) and telomere-proximal (Tel) sides are shown. For Y' elements,
477 adjacent regions equal to half the size of the Y' element are shown. Genome averages are
478 denoted by gray horizontal dashed lines, and colored solid lines with shaded areas represent the
479 mean and two-sided 95% confidence intervals for each protein. **(f)** Bar plots comparing Rec8,
480 Hop1, and Red1 levels on X elements in X-only and XY' ends. Normality of the data was assessed
481 using the Shapiro-Wilk test. Significance was determined using Student's two-sided t-test (*$p \leq$
482 0.05) (raw p-values: 0.0186, 0.0058, 0.0079), with Benjamini-Hochberg p-value adjustment (BH
483 corrected p-values: 0.0186, 0.0118, 0.0118). Effect sizes were estimated using Cohen's d: Rec8
484 (d = 1.62), Hop1 (d = 1.13), and Red1 (d = 0.89). All the data presented here are averages of two
485 independent biological replicates, and the results were reproducible between replicates.

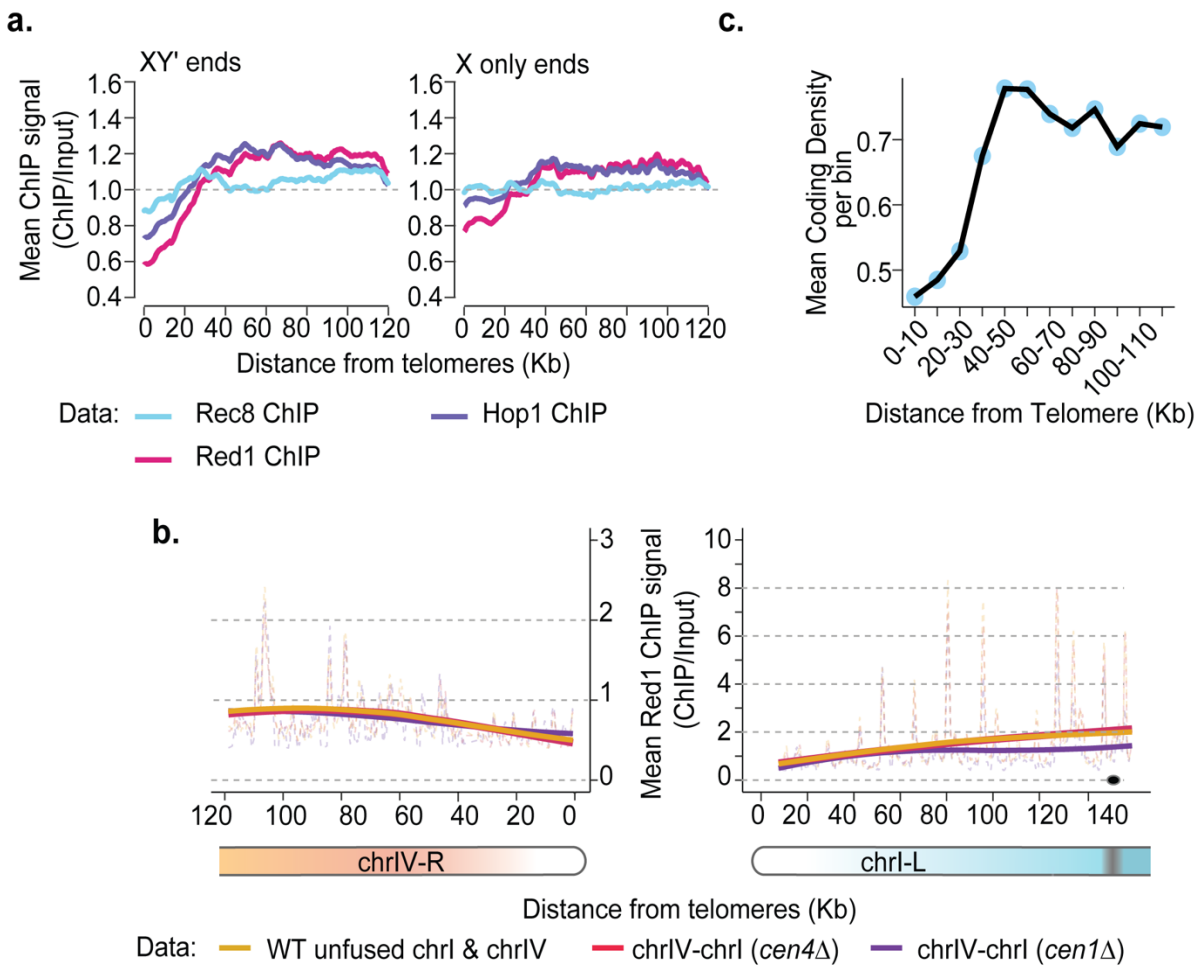

Raghavan *et al*, Fig. 2

Fig. 2: Multiple *cis*-acting features contribute to axis protein depletion near telomeres. (a) Meta-plots of Rec8, Hop1, and Red1 ChIP enrichment (ChIP/Input) at XY' and X-only chromosome ends, aligned by their distance from telomeres. The genome-wide average enrichment is indicated by a dashed gray line. Data are derived from published ChIP-seq datasets of WT cells at early prophase I (3 hours)[14,31,34]. **(b)** Analysis of Red1 binding in SK1/S288C hybrids containing unfused (WT) or homozygous fusion (chrIV-chrI) chromosomes, using published datasets[37]. Dashed lines represent signal traces, and solid-colored lines represent loess-normalized regressions. The black dot marks the position of *CEN1*. **(c)** Coding density as a function of distance from telomeres, averaged across chromosome ends per bin. Blue dots

496 indicate mean coding density per bin, and the black line connects these means. Coding density
497 is calculated as the fraction of DNA encoding open reading frames. All the data presented here
498 are averages of two independent biological replicates, and the results were reproducible between
499 replicates.
500

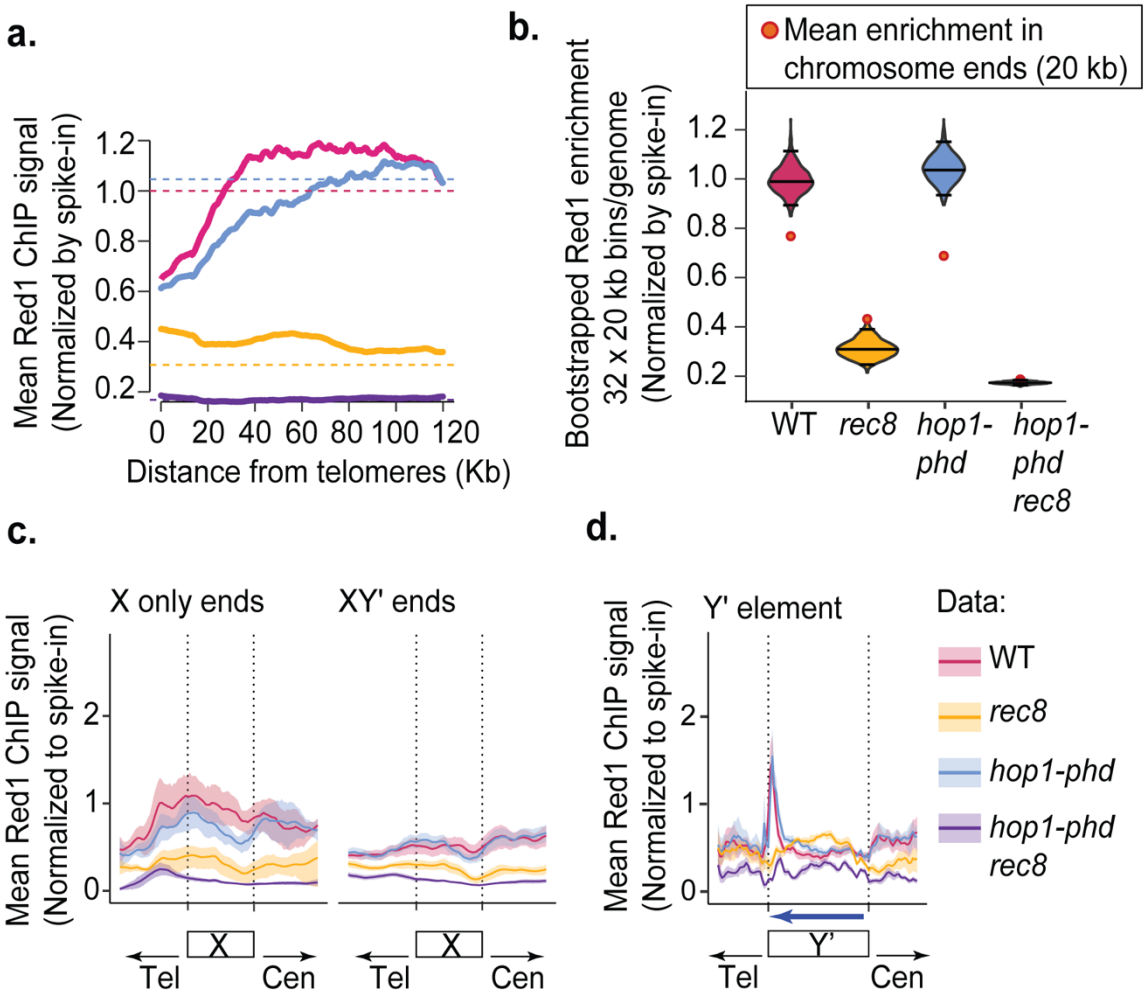

501
502
503 **Fig. 3: Differential recruitment of Red1 at chromosome ends by Rec8-dependent and**
504 **independent pathways. (a)** Meta-plots of average Red1 enrichment (spike-in normalized) at
505 various distances from telomeres in WT, *rec8*, *hop1-phd*, *and hop1-phd rec8* strains during early
506 prophase I (3 hours). Data are derived from spike-in normalized SNP ChIP-seq datasets[15]. The

507 colored dashed lines represent the genome average for each strain after spike-in normalization.
508 **(b)** Bootstrapped distributions of Red1 enrichment within thirty-two 20 kb bins across the genome,
509 with medians and two-sided 95% confidence intervals indicated by black lines. Mean enrichment
510 in the last 20 kb of chromosome ends is highlighted with orange/red circles. **(c, d)** Meta-plots of
511 average Red1 enrichment on X and Y' elements at chromosome ends. Vertical dotted lines mark
512 the positions of X and Y' elements. Adjacent regions—of the same size for X elements or half-
513 sized for Y' elements—are included both telomere (Tel) and centromere (Cen) proximal to the
514 elements. Colored solid lines represent mean enrichment, with shaded areas depicting two-sided
515 95% confidence intervals for each strain. The blue arrow denotes the transcription direction of the
516 Y' ORF. All the data presented here are averages of two independent biological replicates, and
517 the results were reproducible between replicates.
518

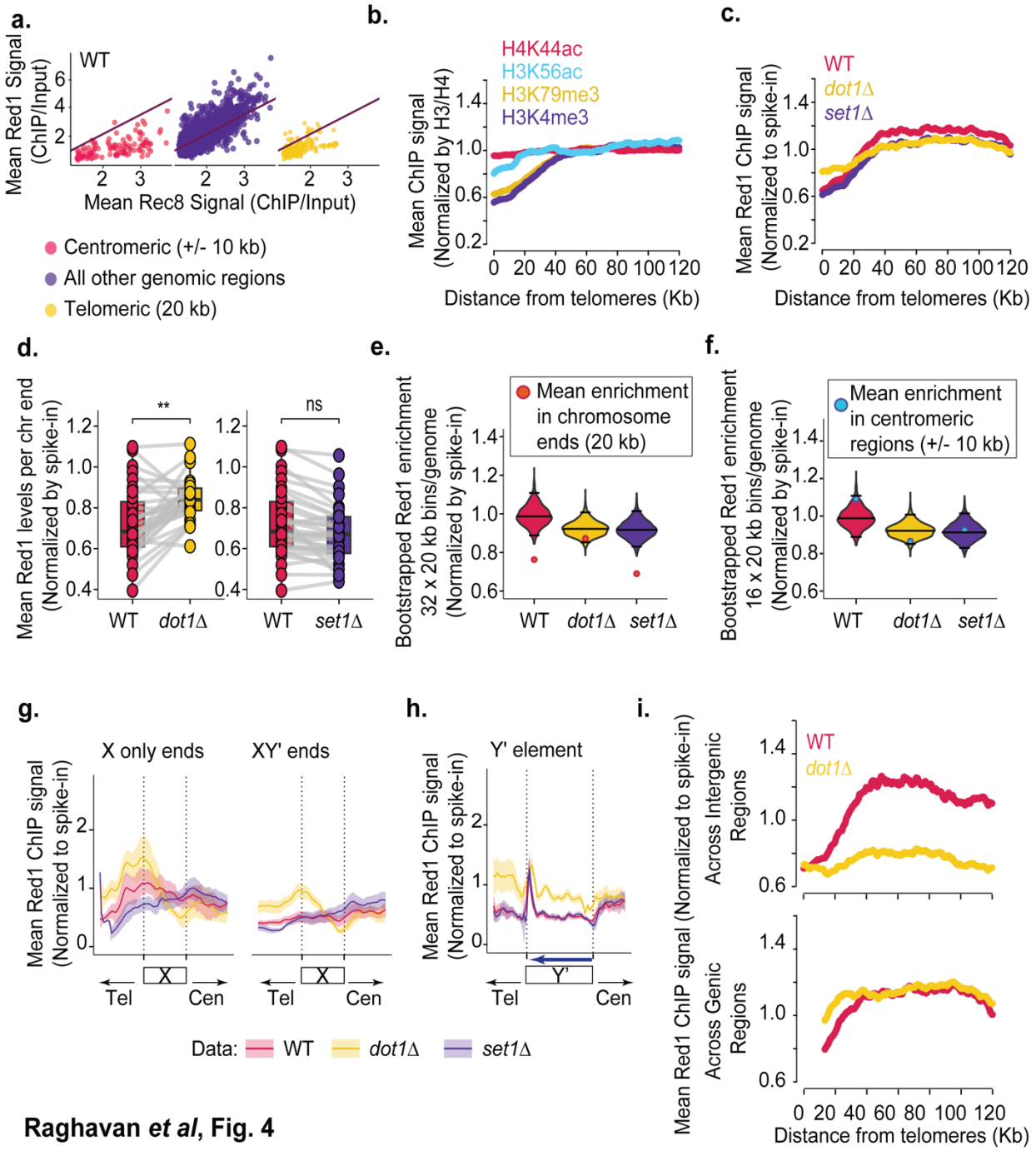

Fig. 4: Dot1 regulates axis protein distribution at chromosome ends and interior regions. **(a)** Scatter plot comparing Red1 and Rec8 levels at individual Rec8 peaks across three genomic regions: pericentromeric regions (±10 kb from centromeres), non-pericentromeric/non-telomeric regions, and chromosome ends (last 20 kb). Genome-wide trend lines illustrate the overall

524 correlation between Red1 and Rec8 (slope of linear regression trendline = 1.34). Data are derived
525 from published WT ChIP-seq datasets[14]. **(b)** Mean histone acetylation and methylation marks
526 (H4K44ac, H3K56ac, H3K4me3, and H3K79me3), normalized to H4 or H3, plotted as a function
527 of distance from chromosome ends using published datasets as well as experimental
528 datasets[42,44]. **(c)** Spike-in normalized Red1 levels in WT, *dot1Δ*, and *set1Δ* mutants, plotted as a
529 function of distance from chromosome ends using published datasets[34]. **(d)** Boxplots of mean
530 Red1 levels per chromosome end (20 kb) in WT, *dot1Δ*, and *set1Δ* mutants. Circles represent
531 mean signals for individual chromosome ends, with lines connecting matched chromosome ends
532 across strains. Normality of the data was assessed using the Shapiro-Wilk test. Student's two-
533 sided t-test **$p \leq 0.01$, ns – non significant (raw p-values: 0.001891863, 0.181274230), Benjamini-
534 Hochberg p-value adjusted (BH corrected p-values: 0.003783726, 0.181274230). Effect sizes
535 were estimated using Cohen's d: WT vs. *dot1Δ* (d = -0.82); WT vs. *set1Δ* (d = 0.34). **(e, f)**
536 Bootstrapped distributions of Red1 enrichment within (e) thirty-two 20 kb bins and (f) sixteen 20
537 kb bins, spanning the genome. Median values and two-sided 95% confidence intervals are shown
538 as black horizontal lines. Orange/red circles in **(e)** indicate mean enrichment at the last 20 kb of
539 chromosome ends, and blue circles in **(f)** highlight mean enrichment at ±10 kb around
540 centromeres. **(g, h)** Meta-plots of Red1 enrichment on X and Y' elements. Vertical dotted lines
541 indicate the positions of X and Y' elements. Adjacent regions, of the same size for X elements or
542 half-sized for Y' elements, are shown telomere (Tel) and centromere (Cen) proximal. Colored
543 solid lines represent mean enrichment, with shaded areas showing two-sided 95% confidence
544 intervals for each strain. The blue arrow denotes the transcription direction of the Y' ORF. **(i)** Meta-
545 analysis of Red1 distribution in WT and *dot1Δ* mutants, separated into intergenic (top panel) and
546 genic regions (bottom panel), plotted as a function of distance from chromosome ends using
547 spike-in normalized values. All the data presented here are averages of two independent
548 biological replicates, and the results were reproducible between replicates.

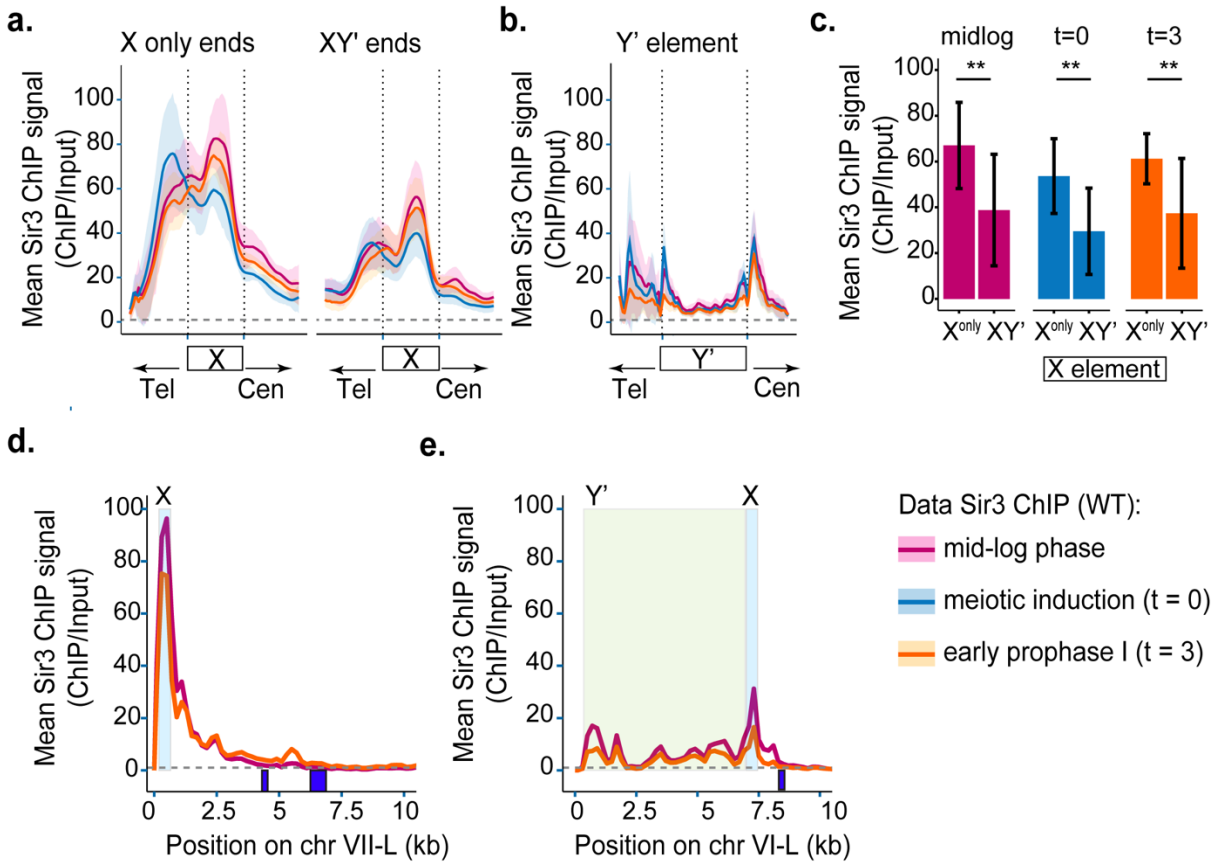

Raghavan *et al*, Figure 5

Fig. 5: Sir3 spreads heterogeneously from the X element during meiotic prophase I. (a, b) Meta-plots of Sir3 ChIP enrichment in wild-type (WT) strains at X elements and Y' elements during mid-log phase, meiotic induction (time = 0 hours), and early prophase I (time = 3 hours). Vertical dotted lines indicate the positions of X and Y' elements. Adjacent regions—of the same size for X elements or half-sized for Y' elements—are shown both telomere (Tel) and centromere (Cen) proximal. **(c)** Bar plots comparing Sir3 enrichment at X elements in X-only and XY' chromosome ends during mid-log phase, meiotic induction (time = 0 hours), and early prophase I (time = 3 hours). Normality of the data was assessed using the Shapiro-Wilk test. Student's two-sided t-test **$p \leq 0.01$ (raw p-values: 0.007263657, 0.007243783, 0.001837521), Benjamini-Hochberg p-value adjusted (BH corrected p-values: 0.007263657, 0.007263657, 0.005512564). Effect sizes were estimated using Cohen's d: Sir3 mid-log phase (d = 1.22); meiotic induction (d = 1.32); early

561 prophase I (d = 1.11). **(d, e)** Sir3 binding profiles on chrVII-L **(d)** and chrVI-L **(e)** during mid-log
562 phase and early meiotic prophase I (time = 3 hours). ChrVII-L shows detectable spreading of Sir3
563 from the X element into adjacent gene-poor regions, while no detectable spreading is observed
564 on chrVI-L. ORFs are annotated in blue. All the data presented here are averages of two
565 independent biological replicates, and the results were reproducible between replicates.

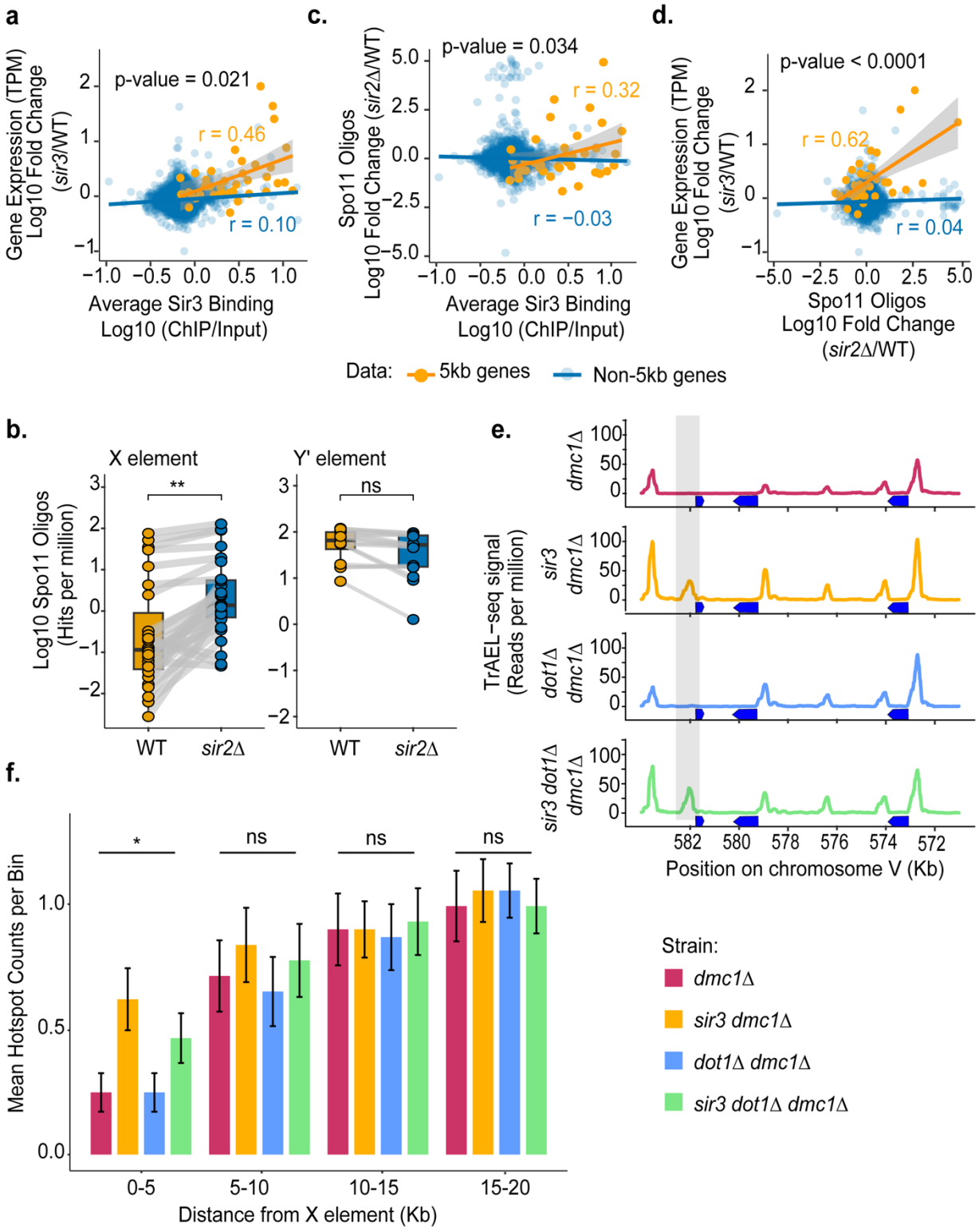

566 **Raghavan *et al*, Fig. 6**

567 **Fig. 6: Sir proteins protect X elements and regions of spread from meiotic DSBs. (a)** Scatter
568 plot of gene expression fold change (*sir3*/WT, measured in *ndt80Δ* background) versus Sir3
569 binding (log10 ChIP/Input) in promoter regions for 5 kb genes (yellow) and non-5 kb genes (blue)
570 at 3 hours post-meiotic induction. Pearson correlation coefficients (r) were calculated in R using
571 the cor() function (Pearson method) and serve as the measure of effect size. p-values were
572 computed using Fisher Z-transformation (two-sided test) to enable statistical testing of correlation
573 significance. Outliers (top and bottom 1% quantiles for 5 kb genes and three non-5 kb gene
574 outliers) were excluded. **(b)** Boxplots of log10-transformed Spo11-oligo signals (hits per million)
575 at X and Y' elements in WT and s*ir2Δ* strains. Data are derived from published Spo11-oligo
576 datasets[29,50]. Circles represent total scores for individual elements, with lines connecting matched
577 elements across strains. Normality of the data was assessed using the Shapiro-Wilk test. Since
578 the data did not meet normality assumptions, the Wilcoxon rank-sum test was used to compare
579 groups. Wilcoxon rank-sum test (two-sided) **$p \leq 0.01$; ns - not significant (raw p-values:
580 0.00179054, 0.15670080), with Benjamini-Hochberg p-value adjustment (BH adjusted p-values:
581 0.003581081, 0.156700804). Effect sizes were estimated using Rank-Biserial Correlation (RBC)
582 ($r = -0.707, -0.408$). **(c)** Scatter plot of Spo11-oligo fold change (*sir2Δ*/WT) in promoter regions as
583 a function of average Sir3 binding (log10 ChIP/Input) in the same promoter regions. Yellow points
584 represent genes within 5 kb of X elements, and blue points represent non-5 kb genes. Pearson
585 correlation coefficients (r) serve as the measure of effect size, and p-values were computed as in
586 (a). Outliers (top and bottom 1% quantiles for 5 kb genes and three outliers from non-5 kb genes)
587 were excluded. **(d)** Scatter plot of gene expression fold change (*sir3*/WT, measured in *ndt80Δ*
588 strains) as a function of Spo11-oligo fold change (*sir2Δ*/WT) in promoter regions for genes within
589 5 kb of X elements (yellow) and non-5 kb genes (blue). Pearson correlation coefficients (r) serve
590 as the measure of effect size, and p-values were computed as in (a). **(e)** TrAEL-seq signal tracks
591 for chromosome V-R subtelomeric regions in the indicated strains. Blue boxes represent

592 annotated ORFs. The highlighted region (gray) marks a peak present in *sir3 dmc1Δ* and *sir3*
593 *dot1Δ dmc1Δ* but absent in *dmc1Δ* and *dot1Δ dmc1Δ*. **(f)** Mean hotspot counts per 5 kb bin as a
594 function of distance from X elements for the indicated strains. Hotspots were identified using
595 peaks called as significant from TrAEL-seq data. Error bars represent the standard error of the
596 mean. Normality of the data was assessed using the Shapiro-Wilk test. Since the data did not
597 meet normality assumptions, the Wilcoxon rank-sum test was used to compare groups. Statistical
598 significance was assessed using a Kruskal-Wallis two-sided test to compare hotspot counts
599 across bins. *p ≤ 0.05; ns - not significant (Raw p-values: 0.04066, 0.8046, 0.9805, 0.9118). All
600 the data presented here are averages of two independent biological replicates, and the results
601 were reproducible between replicates.
602

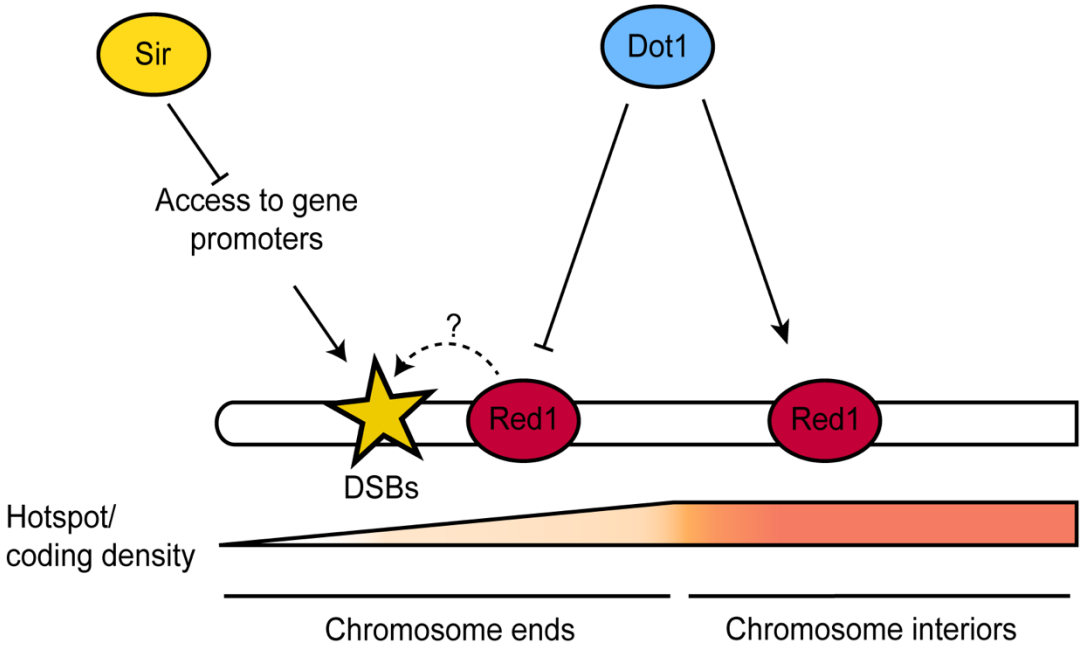

603 **Raghavan *et al*, Fig. 7**

604 **Fig. 7: Model showing distinct mechanisms of DSB regulation at chromosome ends by Sir3**
605 **and Dot1**. Sir proteins restrict promoter accessibility at chromosome ends, thereby influencing
606 DSB formation in these regions. In contrast, Dot1 prevents Red1 accumulation at chromosome
607 ends by directing it to chromosome interiors. Whether the decreased Red1 levels contribute to
608 lower DSB levels or increased sister repair at chromosome ends similar to the rest of the genome
609 remains unresolved (dashed line with a question mark). Orange shading represents
610 coding/hotspot density.

611 **References:**

612 1. Mozzachiodi, S. & Liti, G. Evolution of yeast hybrids by aborted meiosis. *Current Opinion*
613 *in Genetics and Development* **77**, 101980-101980 (2022).
614 2. Börner, G.V., Hochwagen, A. & MacQueen, A.J. Meiosis in budding yeast. *Genetics* **225**,
615 1-33 (2023).
616 3. Duro, E. & Marston, A.L. From equator to pole: Splitting chromosomes in mitosis and
617 meiosis. *Genes and Development* **29**, 109-122 (2015).
618 4. Hunter, N. Meiotic recombination: The essence of heredity. *Cold Spring Harbor*
619 *Perspectives in Biology* **7**(2015).
620 5. Arter, M. & Keeney, S. Divergence and conservation of the meiotic recombination
621 machinery. *Nature Reviews Genetics* **25**, 309-325 (2024).
622 6. Lichten, M. Meiotic chromatin: The substrate for recombination initiation. *Genome*
623 *Dynamics and Stability* **3**, 165-193 (2008).
624 7. Raghavan, A.R. & Hochwagen, A. Keeping it safe: control of meiotic chromosome
625 breakage. *Trends in Genetics* (2024).
626 8. Ito, M. & Shinohara, A. Chromosome architecture and homologous recombination in
627 meiosis. *Front Cell Dev Biol* **10**, 1097446 (2022).
628 9. Mohibullah, N. & Keeney, S. Numerical and spatial patterning of yeast meiotic DNA
629 breaks by Tel1. *Genome Research* **27**(2017).
630 10. Pan, J. *et al.* A hierarchical combination of factors shapes the genome-wide topography
631 of yeast meiotic recombination initiation. *Cell* **144**, 719-731 (2011).
632 11. Panizza, S. *et al.* Spo11-accessory proteins link double-strand break sites to the
633 chromosome axis in early meiotic recombination. *Cell* **146**, 372-383 (2011).
634 12. Schwacha, A. & Kleckner, N. Interhomolog Bias during Meiotic Recombination: Meiotic
635 Functions Promote a Highly Differentiated Interhomolog-Only Pathway. in *Cell* Vol. 90
636 1123-1135 (Keeney and Kleckner, 1997).
637 13. Hollingsworth, P.L. Making it Through Parenting. *Gifted Child Today Magazine* **13**, 2-7
638 (1990).
639 14. Sun, X. *et al.* Transcription dynamically patterns the meiotic chromosome-axis interface.
640 *eLife* **4**, 1-23 (2015).
641 15. Heldrich, J. *et al.* Two pathways drive meiotic chromosome axis assembly in
642 *Saccharomyces cerevisiae*. *Nucleic Acids Research* **50**, 4545-4556 (2022).
643 16. Joshi, N., Barot, A., Jamison, C. & Börner, G.V. Pch2 links chromosome axis remodeling
644 at future crossover sites and crossover distribution during yeast meiosis. *PLoS Genet* **5**,
645 e1000557 (2009).
646 17. Milano, C.R. *et al.* Chromatin binding by HORMAD proteins regulates meiotic
647 recombination initiation. *EMBO Journal* **43**, 836-867 (2024).
648 18. Blitzblau, H.G., Bell, G.W., Rodriguez, J., Bell, S.P. & Hochwagen, A. Mapping of Meiotic
649 Single-Stranded DNA Reveals Double-Strand-Break Hotspots near Centromeres and
650 Telomeres. *Current Biology* **17**, 2003-2012 (2007).
651 19. Sasaki, M., Lange, J. & Keeney, S. Genome destabilization by homologous recombination
652 in the germ line. *Nature Reviews Molecular Cell Biology* **11**, 182-195 (2010).

653 20. Ross, L.O., Maxfield, R. & Dawson, D. Exchanges are not equally able to enhance meiotic
654 chromosome segregation in yeast. *Proceedings of the National Academy of Sciences of*
655 *the United States of America* **93**(1996).
656 21. Oliver, T.R. *et al.* New insights into human nondisjunction of chromosome 21 in oocytes.
657 *PLoS Genet* **4**, e1000033 (2008).
658 22. Ghosh, S., Feingold, E. & Dey, S.K. Etiology of Down syndrome: Evidence for consistent
659 association among altered meiotic recombination, nondisjunction, and maternal age
660 across populations. *Am J Med Genet A* **149a**, 1415-20 (2009).
661 23. Pryde, F.E., Gorham, H.C. & Louis, E.J. Chromosome ends: all the same under their caps.
662 *Curr Opin Genet Dev* **7**, 822-8 (1997).
663 24. Louis, E.J. The chromosome ends of *Saccharomyces cerevisiae*. *Yeast* **11**, 1553-1573
664 (1995).
665 25. Hocher, A. & Taddei, A. Subtelomeres as Specialized Chromatin Domains. *BioEssays*
666 **42**(2020).
667 26. Fabre, E. & Spichal, M. Subnuclear Architecture of Telomeres and Subtelomeres in Yeast.
668 in *Subtelomeres* (eds. Louis, E.J. & Becker, M.M.) 13-37 (Springer Berlin Heidelberg,
669 Berlin, Heidelberg, 2014).
670 27. Brothers, M. & Rine, J. Distinguishing between recruitment and spread of silent
671 chromatin structures in *Saccharomyces cerevisiae*. *eLife* **11**, 1-23 (2022).
672 28. Hocher, A. *et al.* Expanding heterochromatin reveals discrete subtelomeric domains
673 delimited by chromatin landscape transitions. *Genome Research* **28**, 1852-1866 (2018).
674 29. Buhler, C., Borde, V. & Lichten, M. Mapping meiotic single-strand DNA reveals a new
675 landscape of DNA double-strand breaks in *Saccharomyces cerevisiae*. *PLoS Biology* **5**,
676 2797-2808 (2007).
677 30. Murakami, H. *et al.* Multilayered mechanisms ensure that short chromosomes
678 recombine in meiosis. *Nature* (2020).
679 31. Subramanian, V.V. *et al.* Persistent DNA-break potential near telomeres increases
680 initiation of meiotic recombination on short chromosomes. *Nature Communications* **10**,
681 1-15 (2019).
682 32. Yue, J.X. *et al.* Contrasting evolutionary genome dynamics between domesticated and
683 wild yeasts. *Nature Genetics* **49**, 913-924 (2017).
684 33. D'Angiolo, M. *et al.* Telomeres are shorter in wild *Saccharomyces cerevisiae* isolates than
685 in domesticated ones. *Genetics* **223**(2023).
686 34. Vale-Silva, L.A., Markowitz, T.E. & Hochwagen, A. SNP-ChIP: A versatile and tag-free
687 method to quantify changes in protein binding across the genome. *BMC Genomics* **20**, 1-
688 10 (2019).
689 35. Kwapisz, M. & Morillon, A. Subtelomeric Transcription and its Regulation. *Journal of*
690 *molecular biology* **432**, 4199-4219 (2020).
691 36. Wellinger, R.J. & Zakian, V.A. Everything you ever wanted to know about S*accharomyces*
692 *cerevisiae* telomeres: Beginning to end. *Genetics* **191**, 1073-1105 (2012).
693 37. Luo, J. *et al.* Synthetic chromosome fusion: Effects on mitotic and meiotic genome
694 structure and function. *Cell Genomics* **3**(2023).
695 38. Glynn, E.F. *et al.* Genome-wide mapping of the cohesin complex in the yeast
696 *Saccharomyces cerevisiae. PLoS Biology* **2**(2004).

697 39. Ocampo-Hafalla, M.T. & Uhlmann, F. Cohesin loading and sliding. *Journal of Cell Science*
698 **124**, 685-691 (2011).
699 40. Bausch, C. *et al.* Transcription Alters Chromosomal Locations of Cohesin in
700 *Saccharomyces cerevisiae*. *Molecular and Cellular Biology* **27**, 8522-8532 (2007).
701 41. Borde, V. *et al.* Histone H3 lysine 4 trimethylation marks meiotic recombination
702 initiation sites. *EMBO Journal* **28**, 99-111 (2009).
703 42. Hu, J. *et al.* H4K44 Acetylation Facilitates Chromatin Accessibility during Meiosis. *Cell*
704 *Reports* **13**, 1772-1780 (2015).
705 43. Gothwal, S.K. *et al.* The double-strand break landscape of meiotic chromosomes is
706 shaped by the Paf1 transcription elongation complex in *Saccharomyces cerevisiae*.
707 *Genetics* **202**, 497-512 (2016).
708 44. Zhu, X. & Keeney, S. High-resolution global analysis of the influences of Bas1 and Ino4
709 transcription factors on meiotic DNA break distributions in *saccharomyces cerevisiae*.
710 *Genetics* **201**, 525-542 (2015).
711 45. Bani Ismail, M., Shinohara, M. & Shinohara, A. Dot1-dependent histone H3K79
712 methylation promotes the formation of meiotic double-strand breaks in the absence of
713 histone H3K4 methylation in budding yeast. *PLoS ONE* **9**(2014).
714 46. Takahashi, Y.-H. *et al.* Dot1 and Histone H3K79 Methylation in Natural Telomeric and
715 HM Silencing. *Molecular Cell* **42**, 118-126 (2011).
716 47. Shilatifard, A. Chromatin modifications by methylation and ubiquitination: Implications
717 in the regulation of gene expression. *Annual Review of Biochemistry* **75**, 243-269 (2006).
718 48. San-Segundo, P.A. & Roeder, G.S. Role for the Silencing Protein Dot1 in Meiotic
719 Checkpoint Control. in *Molecular Biology of the Cell* Vol. 11 3601-3615 (2000).
720 49. Hoppe, G.J. *et al.* Steps in Assembly of Silent Chromatin in Yeast: Sir3-Independent
721 Binding of a Sir2/Sir4 Complex to Silencers and Role for Sir2-Dependent Deacetylation.
722 *Molecular and Cellular Biology* **22**, 4167-4180 (2002).
723 50. Rusche, L.N., Kirchmaier, A.L. & Rine, J. The Establishment, Inheritance, and Function of
724 Silenced Chromatin in *Saccharomyces cerevisiae*. *Annual Review of Biochemistry* **72**,
725 481-516 (2003).
726 51. Pryde, F.E. & Louis, E.J. Limitations of silencing at native yeast telomeres. *EMBO Journal*
727 **18**, 2538-2550 (1999).
728 52. Thacker, D., Mohibullah, N., Zhu, X. & Keeney, S. Homologue engagement controls
729 meiotic DNA break number and distribution. *Nature* **510**, 241-246 (2014).
730 53. Kara, N., Krueger, F., Rugg-Gunn, P. & Houseley, J. Genome-wide analysis of DNA
731 replication and DNA double-strand breaks using TrAEL-seq. *PLoS Biology* **19**(2021).
732 54. Bishop, D.K., Park, D., Xu, L. & Kleckner, N. *DMC1*: A meiosis-specific yeast homolog of E.
733 coli *recA* required for recombination, synaptonemal complex formation, and cell cycle
734 progression. *Cell* **69**, 439-456 (1992).
735 55. Vader, G. *et al.* Protection of repetitive DNA borders from self-induced meiotic
736 instability. *Nature* **477**, 115-121 (2011).
737 56. Fourel, G., Revardel, E., Koering, C.E. & Gilson, É. Cohabitation of insulators and silencing
738 elements in yeast subtelomeric regions. *EMBO Journal* **18**, 2522-2537 (1999).
739 57. Radman-Livaja, M. *et al.* Dynamics of Sir3 spreading in budding yeast: Secondary
740 recruitment sites and euchromatic localization. *EMBO Journal* **30**, 1012-1026 (2011).

741 58. Fourel, G. *et al.* An activation-independent role of transcription factors in insulator
742 function. in *EMBO reports* Vol. 2 124-132 (2001).
743 59. Saxton, D.S. & Rine, J. Nucleosome Positioning Regulates the Establishment, Stability,
744 and Inheritance of Heterochromatin in *Saccharomyces cerevisiae*. *PNAS* **117**, 27493-
745 27501 (2004).
746 60. Ichikawa, Y., Morohashi, N., Nishimura, Y., Kurumizaka, H. & Shimizu, M. Telomeric
747 repeats act as nucleosome-disfavouring sequences in vivo. *Nucleic Acids Research* **42**,
748 1541-1552 (2014).
749 61. Markowitz, T.E. *et al.* Reduced dosage of the chromosome axis factor Red1 selectively
750 disrupts the meiotic recombination checkpoint in *Saccharomyces cerevisiae*. *PLoS*
751 *Genetics* **13**(2017).
752 62. Su, Y., Barton, A.B. & Kaback, D.B. Decreased meiotic reciprocal recombination in
753 subtelomeric regions in *Saccharomyces cerevisiae*. *Chromosoma* **109**, 467-475 (2000).
754 63. Lamb, N.E., Yu, K., Shaffer, J., Feingold, E. & Sherman, S.L. Association between maternal
755 age and meiotic recombination for trisomy 21. *American Journal of Human Genetics* **76**,
756 91-99 (2005).
757 64. Sherman, S.L., Freeman, S.B., Allen, E.G. & Lamb, N.E. Risk factors for nondisjunction of
758 trisomy 21. *Cytogenetic and Genome Research* **111**, 273-280 (2005).
759 65. Humphryes, N. & Hochwagen, A. A non-sister act: Recombination template choice
760 during meiosis. *Experimental Cell Research* **329**, 53-60 (2014).
761 66. Medhi, D., Goldman, A.S. & Lichten, M. Local chromosome context is a major
762 determinant of crossover pathway biochemistry during budding yeast meiosis. (2016).
763 67. Scherthan, H. A bouquet makes ends meet. *Nature Reviews Molecular Cell Biology* **2**,
764 621-627 (2001).
765 68. Blitzblau, H.G. & Hochwagen, A. ATR/Mec1 prevents lethal meiotic recombination
766 initiation on partially replicated chromosomes in budding yeast. *eLife* **2**, 1-20 (2013).
767 69. Langmead, B. & Salzberg, S.L. Fast gapped-read alignment with Bowtie 2. *Nature*
768 *Methods* **9**, 357-359 (2012).
769 70. Kar, F.M., Vogel, C. & Hochwagen, A. Meiotic DNA breaks activate a streamlined
770 phospho-signaling response that largely avoids protein-level changes. *Life Science*
771 *Alliance* **5**, 1-15 (2022).
772 71. Ewels, P.A.P.A.F.S. & et al. The nf-core framework for community-curated bioinformatics
773 pipelines. *Nature Biotechnology* **38**, 271-271 (2020).
774 72. Patel H, E.P.P.A.H.n.R.B.O.S.G.M.D.V.P.M.S.L. & et al. nf-core/rnaseq: Nf-core/ rnaseq
775 v3.1 - Lead Alligator (3.1). (2021).
776 73. Patro, R., Duggal, G., Love, M.I., Irizarry, R.A. & Kingsford, C. Salmon provides fast and
777 bias-aware quantification of transcript expression. *Nature Methods* **14**, 417-419 (2017).
778 74. Heldrich, J., Sun, X., Vale-Silva, L.A., Markowitz, T.E. & Hochwagen, A. Topoisomerases
779 Modulate the Timing of Meiotic DNA Breakage and Chromosome Morphogenesis in
780 *Saccharomyces cerevisiae*. *Genetics* **215**, 59-73 (2020).
781